

# $k$ -Space Deep Learning for Accelerated MRI

Yoseob Han, and Jong Chul Ye\*, *Senior Member, IEEE*

**Abstract**—The annihilating filter-based low-rank Hankel matrix approach (ALOHA) is one of the state-of-the-art compressed sensing approaches that directly interpolates the missing  $k$ -space data using low-rank Hankel matrix completion. Inspired by the recent mathematical discovery that links deep neural networks to Hankel matrix decomposition using data-driven framelet basis, here we propose a fully data-driven deep learning algorithm for  $k$ -space interpolation. Our network can be also easily applied to non-Cartesian  $k$ -space trajectories by simply adding an additional re-gridding layer. Extensive numerical experiments show that the proposed deep learning method significantly outperforms the existing image-domain deep learning approaches.

**Index Terms**—Compressed sensing MRI,  $k$ -space, Deep Learning, Hankel structured low-rank completion, Deep convolutional framelets

## I. INTRODUCTION

RECENTLY, inspired by the tremendous success of deep learning in classification [1], [2] and low-level computer vision problems [3]–[5], many researchers have investigated deep learning approaches for various biomedical image reconstruction problems and successfully demonstrated significant performance gain [6]–[13].

In MR literature, the works in [14]–[16] were among the first that applied deep learning approaches to compressed sensing MRI (CS-MRI). In particular, Wang et al [14] used the deep learning reconstruction either as an initialization or a regularization term. Deep network architecture using unfolded iterative compressed sensing (CS) algorithm was also proposed [15]. Instead of using handcrafted regularizers, the authors in [15] tried to learn a set of regularizers under a variational framework. Multilayer perceptron was introduced in [16] for accelerated parallel MRI. These works were followed by novel extension using deep residual learning [17], domain adaptation [18], data consistency layers [19], cyclic consistency [20], etc. An extreme form of the neural network called AUTomated TransfORM by Manifold APproximation (AUTOMAP) [21] even attempts to estimate the Fourier transform itself using fully connected layers. All these pioneering works have consistently demonstrated superior reconstruction performances over the compressed sensing approaches [22]–[31] at significantly lower run-time computational complexity.

In spite of such intriguing performance improvement by deep learning approaches for reconstruction problems, the theoretical origin of the success is poorly understood. Most prevailing explanations are either to interpret a deep network as unrolled iterative steps from variation optimization

Authors are with the Department of Bio and Brain Engineering, Korea Advanced Institute of Science and Technology (KAIST), Daejeon 34141, Republic of Korea (e-mail: {hanyoseob,jong.ye}@kaist.ac.kr). This work is supported by Korea Science and Engineering Foundation, Grant number NRF2016R1A2B3008104.

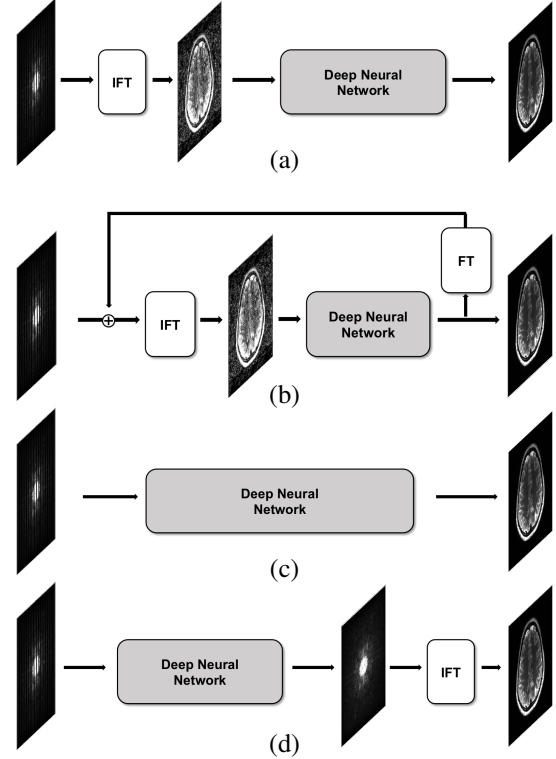


Fig. 1: Deep learning frameworks for accelerated MRI: (a) image domain learning [16]–[18], (b) cascaded network [14], [15], [19], [20], (c) AUTOMAP [21], and (d) the proposed  $k$ -space learning. IFT: Inverse Fourier transform.

framework [15], or regard it as a generative model or an abstract form of manifold learning [21]. However, none of the approaches fully disclose the blackbox nature of the deep network. For example, to the best of our knowledge, we do not have complete answers to the following MR-specific questions:

- 1) What is the optimal way of handling complex-valued MR data set ?
- 2) What is the role of the nonlinearity such as rectified linear unit (ReLU) for the complex-valued data ?
- 3) How many channels do we need ?

Furthermore, the most troubling issue for MR community is that the link to the classical MR image reconstruction approaches is still not fully understood. For example, compressed sensing (CS) theory [32], [33] has been extensively studied for MR image reconstruction from undersampled  $k$ -space samples by imposing sparsity [22]–[25]. The structured low-rank matrix completion algorithms [26]–[31] were proposed as the state-of-the-art algorithms in CS-MRI to achieve significant performance improvement. In particular, the annihilating filter-based low-rank Hankel matrix approach (ALOHA) [28]–[30],

[34] converts the CS-MRI problems to  $k$ -space interpolation problems by exploiting the sparsity. However, to the best of our knowledge, there are no successful deep learning algorithms that can directly interpolate the missing  $k$ -space data in a completely data-driven manner.

Although the end-to-end recovery approach like AUTOMAP [21] may directly recover the image without ever interpolating the missing  $k$ -space samples (see Fig. 1(c)), it works only for the sufficiently small size images due to its huge memory requirement for fully connected layers, since the required memory size is determined by the number of samples in the  $k$ -space multiplied by the number of image domain pixels. Accordingly, most of the popular deep learning MR reconstruction algorithms are either in the form of image domain post-processing as shown in Fig. 1(a) [16]–[18], or iterative updates between the  $k$ -space and the image domain using a cascaded network as shown in Fig. 1(b) [14], [15], [19], [20].

Therefore, one of the main purposes of this paper is to reveal that the aforementioned approaches are not all the available options for MR deep learning, but there exists another much more effective deep learning approach to address these open questions. In fact, as illustrated in Fig. 1(d), the proposed deep learning approach directly interpolates the missing  $k$ -space data so that accurate reconstruction can be obtained by simply taking the Fourier transform of the interpolated  $k$ -space data. Although this concept is simple and may have been tried by many groups, we show that the main reason for the lack of successful algorithms may be due to the ignorance of the link between the deep learning and low-rank Hankel structured matrix approach.

Specifically, the recent theory of deep convolutional framelets [35] showed that an encoder-decoder network emerges from the data-driven low-rank Hankel matrix decomposition [35], whose rank structure is controlled by the number of filter channels. This discovery gives us important clues to develop a successful deep learning approach for  $k$ -space interpolation. We further show that our deep learning approach for  $k$ -space interpolation is so general that it can handle general  $k$ -space sampling patterns beyond the Cartesian trajectory, such as radial, spiral, etc. Moreover, all the network are implemented in the form of convolutional neural network (CNN) without requiring fully connected layer, so the GPU memory requirement is minimal.

## II. MATHEMATICAL PRELIMINARIES

### A. Notations

In this paper, matrices are denoted by bold upper case letters, i.e.  $\mathbf{A}$ ,  $\mathbf{B}$ , whereas the vectors are represented by bold lower case letters, i.e.  $\mathbf{x}$ ,  $\mathbf{y}$ . In addition,  $[\mathbf{A}]_{ij}$  refers to the  $(i, j)$ -th element of the matrix  $\mathbf{A}$ , and  $[\mathbf{x}]_j$  denotes the  $j$ -th element of the vector  $\mathbf{x}$ . The notation  $\bar{\mathbf{v}} \in \mathbb{R}^p$  for a vector  $\mathbf{v} \in \mathbb{R}^d$  denotes its flipped version, i.e. the indices of  $\mathbf{v}$  are reversed. The  $N \times N$  identity matrix is denoted as  $\mathbf{I}_N$ , while  $\mathbf{1}_N$  is an  $N$ -dimensional vector with 1's. The superscript  $T$  and  $\top$  for a matrix or vector denote the transpose and Hermitian transpose, respectively.  $\mathbb{R}$  and  $\mathbb{C}$  denote the real and imaginary fields, respectively.  $\mathbb{R}_+$  refers to the nonnegative real numbers.

### B. Forward Model for Accelerated MRI

The spatial Fourier transform of an arbitrary smooth function  $x : \mathbb{R}^2 \rightarrow \mathbb{R}$  is defined by

$$\hat{x}(\mathbf{k}) = \mathcal{F}[x](\mathbf{k}) := \int_{\mathbb{R}^d} e^{-i\mathbf{k}\cdot\mathbf{r}} x(\mathbf{r}) d\mathbf{r},$$

with spatial frequency  $\mathbf{k} \in \mathbb{R}^2$  and  $i = \sqrt{-1}$ . Let  $\{\mathbf{k}_n\}_{n=1}^N$ , for some integer  $N \in \mathbb{N}$ , be a collection of finite number of sampling points of the  $k$ -space conforming to the Nyquist sampling rate. Accordingly, the discretized  $k$ -space data  $\hat{\mathbf{x}} \in \mathbb{C}^N$  is introduced by

$$\hat{\mathbf{x}} = [\hat{x}(\mathbf{k}_1) \quad \cdots \quad \hat{x}(\mathbf{k}_N)]^T. \quad (1)$$

For a given under-sampling pattern  $\Lambda$  for accelerated MR acquisition, let the downsampling operator  $\mathcal{P}_\Lambda : \mathbb{C}^N \rightarrow \mathbb{C}^N$  be defined as

$$[\mathcal{P}_\Lambda[\hat{\mathbf{x}}]]_j = \begin{cases} [\hat{\mathbf{x}}]_j & j \in \Lambda \\ 0, & \text{otherwise} \end{cases}. \quad (2)$$

Then, the under-sampled  $k$ -space data is given by

$$\hat{\mathbf{y}} := \mathcal{P}_\Lambda[\hat{\mathbf{x}}] \quad (3)$$

### C. ALOHA

Then, CS-MRI [22]–[25] attempts to find the feasible solution that has minimum non-zero support in some sparsifying transform domain. This can be achieved by finding the smooth function  $z : \mathbb{R}^2 \rightarrow \mathbb{R}$  such that

$$\begin{aligned} & \min_z \quad \|\mathcal{T}z\|_1 \\ & \text{subject to} \quad \mathcal{P}_\Lambda[\hat{\mathbf{x}}] = \mathcal{P}_\Lambda[\hat{\mathbf{z}}] \end{aligned} \quad (4)$$

where  $\mathcal{T}$  denotes the image domain sparsifying transform and

$$\hat{\mathbf{z}} = [\hat{z}(\mathbf{k}_1) \quad \cdots \quad \hat{z}(\mathbf{k}_N)]^T. \quad (5)$$

This optimization problem usually requires iterative update between the  $k$ -space and the image domain after the discretization of  $z(\mathbf{r})$  [22]–[25].

Although ALOHA [28], [29] still exploits the image domain sparsifying transform as the conventional CS-MRI algorithms, in contrast to the CS-MRI approaches ALOHA is concerned with the direct  $k$ -space interpolation. More specifically, let  $\mathbb{H}_d(\hat{\mathbf{x}})$  denote a Hankel matrix constructed from the  $k$ -space measurement  $\hat{\mathbf{x}}$  in (1), where  $d$  denotes the matrix pencil size (for more details on the construction of Hankel matrices and their relation to the convolution, see Appendix A in Supplementary Material). According to the theory of ALOHA [28], [34], if the underlying signal  $x(\mathbf{r})$  in the image domain is sparse and described as the signal with the finite rate of innovations (FRI) with rate  $s$  [36], the associated Hankel matrix  $\mathbb{H}_d(\hat{\mathbf{x}})$  with  $d > s$  is low-ranked.

Therefore, if some of  $k$ -space data are missing, we can construct an appropriate weighted Hankel matrix with missing elements such that the missing elements are recovered using low rank Hankel matrix completion approaches [37]–[41]:

$$\begin{aligned} (P) \quad & \min_{\hat{\mathbf{z}} \in \mathbb{C}^N} \quad \text{RANK } \mathbb{H}_d(\hat{\mathbf{z}}) \\ & \text{subject to} \quad \mathcal{P}_\Lambda[\hat{\mathbf{x}}] = \mathcal{P}_\Lambda[\hat{\mathbf{z}}]. \end{aligned} \quad (6)$$

The low-rank Hankel matrix completion problem ( $P$ ) can be solved in various ways, and ALOHA employ the matrix factorization approaches [28]–[30].

ALOHA is extremely useful not only for the accelerated MR acquisitions [28], [29], [31], but also for MR artifact correction [30], [42]. Moreover, it has been used for many low-level computer vision problems [43], [44]. However, the main technical huddle is its relatively large computational complexity for matrix factorization and the memory requirement for storing Hankel matrix. Although several new approaches have been proposed to solve these problems [45], the following section shows that a deep learning approach is a novel and efficient way to solve this problem by making the matrix decomposition completely data-driven and more expressively.

### III. MAIN CONTRIBUTION

#### A. ALOHA with Learned Low-Rank Basis

Consider the following image regression problem under the low-rank Hankel matrix constraint:

$$\min_{\hat{\mathbf{z}} \in \mathbb{C}^N} \left\| x - \mathcal{F}^{-1}[\hat{\mathbf{z}}] \right\|^2 \quad (7)$$

$$\begin{aligned} \text{subject to} \quad & \text{RANK } \mathbb{H}_d(\hat{\mathbf{z}}) = s, \\ & \mathcal{P}_\Lambda[\hat{\mathbf{x}}] = \mathcal{P}_\Lambda[\hat{\mathbf{z}}], \end{aligned} \quad (8)$$

where  $s$  denotes an estimated rank. In the above formulation, the cost in (7) is defined in the image domain to minimize the errors in the image domain, whereas the low-rank Hankel matrix constraint in (8) is imposed in the  $k$ -space after the  $k$ -space weighting.

In order to find the link to the deep learning approaches that are usually implemented in real domain, we convert the complex-valued constraint in (8) to a real-valued constraint. For this, the operator  $\mathfrak{R} : \mathbb{C}^N \rightarrow \mathbb{R}^{N \times 2}$  is defined as

$$\mathfrak{R}[\hat{\mathbf{z}}] := [\text{Re}(\hat{\mathbf{z}}) \quad \text{Im}(\hat{\mathbf{z}})], \quad \forall \hat{\mathbf{z}} \in \mathbb{C}^N \quad (9)$$

where  $\text{Re}(\cdot)$  and  $\text{Im}(\cdot)$  denote the real and imaginary part of the argument. Similarly, we define its inverse operator  $\mathfrak{R}^{-1} : \mathbb{R}^{N \times 2} \rightarrow \mathbb{C}^N$  as

$$\mathfrak{R}^{-1}[\hat{\mathbf{Z}}] := \hat{\mathbf{z}}_1 + \iota \hat{\mathbf{z}}_2, \quad \forall \hat{\mathbf{Z}} := [\mathbf{z}_1 \quad \mathbf{z}_2] \in \mathbb{R}^{N \times 2} \quad (10)$$

Then, as shown in Appendix B in Supplementary Material, we have

$$\begin{aligned} Q &:= \text{RANK} [\text{Re}[\mathbb{H}_d(\hat{\mathbf{z}})] \quad \text{Im}[\mathbb{H}_d(\hat{\mathbf{z}})]] \\ &= \text{RANK} \mathbb{H}_{d|2}(\mathfrak{R}[\hat{\mathbf{z}}]) \leq 2s \end{aligned}$$

if  $\text{RANK} \mathbb{H}_d(\hat{\mathbf{z}}) = s$ . Therefore, (8) can be converted to an optimization problem with real-valued constraint:

$$(P_A) \quad \min_{\hat{\mathbf{z}} \in \mathbb{C}^N} \left\| x - \mathcal{F}^{-1}[\hat{\mathbf{z}}] \right\|^2 \quad (11)$$

$$\begin{aligned} \text{subject to} \quad & \text{RANK} \mathbb{H}_{d|2}(\mathfrak{R}[\hat{\mathbf{z}}]) = Q \leq 2s, \\ & \mathcal{P}_\Lambda[\hat{\mathbf{x}}] = \mathcal{P}_\Lambda[\hat{\mathbf{z}}]. \end{aligned}$$

Although this type of low-rank constraint optimization problem has been addressed via singular value shrinkage or matrix factorization in the classical low-rank Hankel matrix approaches [28]–[31], [42]–[44], one of the most important discoveries

in the deep convolutional framelets [35] is to show that the problem can be addressed using learning-based signal representation.

More specifically, for any  $\hat{\mathbf{z}} \in \mathbb{C}^N$ , let the Hankel structured matrix  $\mathbb{H}_{d|2}(\mathfrak{R}[\hat{\mathbf{z}}])$  have the singular value decomposition  $\mathbf{U}\mathbf{\Sigma}\mathbf{V}^\top$ , where  $\mathbf{U} = [\mathbf{u}_1 \cdots \mathbf{u}_Q] \in \mathbb{R}^{N \times Q}$  and  $\mathbf{V} = [\mathbf{v}_1 \cdots \mathbf{v}_Q] \in \mathbb{R}^{2d \times Q}$  denote the left and the right singular vector bases matrices, respectively;  $\mathbf{\Sigma} = (\sigma_{ij}) \in \mathbb{R}^{Q \times Q}$  is the diagonal matrix with singular values. Now, consider matrix pair  $\mathbf{\Psi}, \tilde{\mathbf{\Psi}} \in \mathbb{R}^{2d \times Q}$

$$\mathbf{\Psi} := \begin{pmatrix} \psi_1^1 & \cdots & \psi_Q^1 \\ \psi_1^2 & \cdots & \psi_Q^2 \end{pmatrix} \quad \text{and} \quad \tilde{\mathbf{\Psi}} := \begin{pmatrix} \tilde{\psi}_1^1 & \cdots & \tilde{\psi}_Q^1 \\ \tilde{\psi}_1^2 & \cdots & \tilde{\psi}_Q^2 \end{pmatrix} \quad (12)$$

that satisfy the low-rank projection constraint:

$$\mathbf{\Psi} \tilde{\mathbf{\Psi}}^\top = \mathbf{P}_{R(\mathbf{V})}, \quad (13)$$

where  $\mathbf{P}_{R(\mathbf{V})}$  denotes the projection matrix to the range space of  $\mathbf{V}$ . We further introduce the generalized pooling and unpooling matrices  $\tilde{\mathbf{\Phi}}, \tilde{\mathbf{\Phi}} \in \mathbb{R}^{N \times M}$  [35] that satisfies the condition

$$\tilde{\mathbf{\Phi}} \tilde{\mathbf{\Phi}}^\top = \mathbf{P}_{R(\mathbf{U})}, \quad (14)$$

Using Eqs. (13) and (14), we can obtain the following matrix equality:

$$\mathbb{H}_{d|2}(\mathfrak{R}[\hat{\mathbf{z}}]) = \tilde{\mathbf{\Phi}} \tilde{\mathbf{\Phi}}^\top \mathbb{H}_{d|2}(\mathfrak{R}[\hat{\mathbf{z}}]) \mathbf{\Psi} \tilde{\mathbf{\Psi}}^\top = \tilde{\mathbf{\Phi}} \mathbf{C} \tilde{\mathbf{\Psi}}^\top, \quad (15)$$

where

$$\mathbf{C} := \tilde{\mathbf{\Phi}}^\top \mathbb{H}_{d|2}(\mathfrak{R}[\hat{\mathbf{z}}]) \mathbf{\Psi} \in \mathbb{R}^{N \times Q} \quad (16)$$

By taking the generalized inverse of Hankel matrix, (15) can be converted to the framelet basis representation with the framelet coefficient  $\mathbf{C}$  in (16) [35] (see Appendix C in Supplementary Material for more details on this framelet basis representation). Moreover, one of the most important observations in [35] is that the framelet basis representation in (15) can be equivalently represented by single layer encoder-decoder convolution architecture:

$$\mathbf{C} = \tilde{\mathbf{\Phi}}^\top (\mathfrak{R}[\hat{\mathbf{z}}] \otimes \tilde{\mathbf{\Psi}}), \quad \mathfrak{R}[\hat{\mathbf{z}}] = (\tilde{\mathbf{\Phi}} \mathbf{C}) \otimes \nu(\tilde{\mathbf{\Psi}}), \quad (17)$$

where  $\otimes$  denotes the multi-channel input multi-channel output convolution. The first and the second part of (17) correspond to the encoder and decoder layers with the corresponding convolution filters  $\tilde{\mathbf{\Psi}} \in \mathbb{R}^{2d \times Q}$  and  $\nu(\tilde{\mathbf{\Psi}}^{(j)}) \in \mathbb{R}^{dQ \times 2}$ :

$$\tilde{\mathbf{\Psi}} := \begin{pmatrix} \bar{\psi}_1^1 & \cdots & \bar{\psi}_Q^1 \\ \bar{\psi}_1^2 & \cdots & \bar{\psi}_Q^2 \\ \tilde{\psi}_1^1 & \cdots & \tilde{\psi}_Q^1 \\ \tilde{\psi}_1^2 & \cdots & \tilde{\psi}_Q^2 \end{pmatrix}, \quad \nu(\tilde{\mathbf{\Psi}}) := \begin{pmatrix} \tilde{\psi}_1^1 & \tilde{\psi}_1^2 \\ \vdots & \vdots \\ \tilde{\psi}_Q^1 & \tilde{\psi}_Q^2 \end{pmatrix},$$

which are obtained by reordering the matrices  $\mathbf{\Psi}$  and  $\tilde{\mathbf{\Psi}}$  in (12). Specifically,  $\bar{\psi}_i^1 \in \mathbb{R}^d$  (resp.  $\bar{\psi}_i^2 \in \mathbb{R}^d$ ) denotes the  $d$ -tap encoder convolutional filter applied to the real (resp. imaginary) component of the  $k$ -space data to generate the  $i$ -th channel output. In addition,  $\nu(\tilde{\mathbf{\Psi}})$  is a reordered version of  $\tilde{\mathbf{\Psi}}$  so that and  $\tilde{\psi}_i^1 \in \mathbb{R}^d$  (resp.  $\tilde{\psi}_i^2 \in \mathbb{R}^d$ ) denotes the  $d$ -tap decoder convolutional filter to generate the real (resp. imaginary) component of the  $k$ -space data by convolving with

the  $i$ -th channel input.

The actual implementation of Eq. (17) is as follows. First, the  $k$ -space data  $\hat{\mathbf{z}}$  are splitted into two channels with the real and imaginary components, respectively. Then, the encoder filters generates  $Q$ -channel outputs from this two channel inputs using multi-channel convolution, after which the pooling operation defined by  $\Phi^\top$  is applied to each  $Q$ -channel output. The resulting  $Q$ -channel feature maps corresponds to the convolutional framelet coefficients. At the decoder, the  $Q$ -channel feature maps are processed using unpooling layer represented by  $\tilde{\Phi}$ , which are then convoluted with the decoder filters to generate real and image channels of the estimated  $k$ -space data. Finally, complex valued  $k$ -space data are formed from the two channel output. Note that the rank structure of the estimated Hankel matrix is hardwired as the number of filter channels, i.e.  $Q$ .

Since (17) is a general form of the signals that are associated with a rank- $Q$  Hankel structured matrix, we are interested in using it to estimate bases for  $k$ -space interpolation. For this, the filters  $\Psi, \tilde{\Psi} \in \mathbb{R}^{2d \times Q}$  should be estimated from the training data. Specifically, we consider the signal space  $\mathcal{H}^0$  spanned by the convolutional framelet basis:

$$\mathcal{H}^0 = \left\{ \mathbf{G} \in \mathbb{R}^{N \times 2} \mid \mathbf{G} = \Phi^\top \left( \mathbf{C} \otimes \nu(\tilde{\Psi}) \right), \right. \\ \left. \mathbf{C} = (\tilde{\Phi} \mathbf{G}) \otimes \bar{\Psi} \right\}. \quad (18)$$

Then, the ALOHA formulation  $P_A$  can be equivalently represented by

$$(P'_A) \quad \min_{\{\hat{\mathbf{z}} \in \mathbb{C}^N \mid \Re[\hat{\mathbf{z}}] \in \mathcal{H}^0\}} \|x - \mathcal{F}^{-1}[\hat{\mathbf{z}}]\|^2 \\ \text{subject to} \quad \mathcal{P}_\Lambda[\hat{\mathbf{x}}] = \mathcal{P}_\Lambda[\hat{\mathbf{z}}],$$

Suppose that we are given training data set  $\{\hat{\mathbf{y}}_{(i)}, x_{(i)}\}_{i=1}^M$ , where  $\hat{\mathbf{y}}_{(i)}$  denotes the under-sampled  $k$ -space data and  $x_{(i)}$  refers to the corresponding ground-truth image. Then, from  $(P'_A)$ , we can obtain the following filter estimation formulation:

$$\min_{\Psi, \tilde{\Psi} \in \mathbb{R}^{2d \times Q}} \sum_{i=1}^M \left\| x_{(i)} - \mathcal{K}(\hat{\mathbf{y}}_{(i)}; \Psi, \tilde{\Psi}) \right\|^2, \quad (19)$$

Here, the operator  $\mathcal{K} : \mathbb{C}^N \rightarrow \mathbb{C}^N$  is defined as

$$\mathcal{K}(\hat{\mathbf{y}}_{(i)}; \Psi, \tilde{\Psi}) = \mathcal{F}^{-1} \left[ \Re^{-1} \left[ \left( \tilde{\Phi} \mathbf{C} \left( \Re[\hat{\mathbf{y}}_{(i)}] \right) \right) \otimes \nu(\tilde{\Psi}) \right] \right]$$

in terms of the mapping  $\mathbf{C} : \mathbb{R}^{N \times 2} \rightarrow \mathbb{R}^{N \times Q}$

$$\mathbf{C}(\hat{\mathbf{G}}) = \Phi^\top \left( \hat{\mathbf{G}} \otimes \bar{\Psi} \right), \quad \forall \hat{\mathbf{G}} \in \mathbb{R}^{N \times 2} \quad (20)$$

After the network is fully trained, the image inference from a downsampled  $k$ -space data  $\hat{\mathbf{y}}$  is simply done by  $\mathcal{K}(\hat{\mathbf{y}}; \Psi, \tilde{\Psi})$ , whereas the interpolated  $k$ -space samples can be obtained by

$$\hat{\mathbf{z}} = \Re^{-1} \left[ \left( \tilde{\Phi} \mathbf{C} \left( \Re[\hat{\mathbf{y}}_{(i)}] \right) \right) \otimes \nu(\tilde{\Psi}) \right].$$

## B. DeepALOHA

The idea can be further extended to the multi-layer deep convolutional framelet expansion. Specially, suppose that the encoder and decoder convolution filter  $\tilde{\Psi}, \nu(\tilde{\Psi}) \in \mathbb{R}^{2d \times Q}$

can be represented in a cascaded convolution of small length filters:

$$\bar{\Psi} = \bar{\Psi}^{(0)} \otimes \dots \otimes \bar{\Psi}^{(J)} \\ \nu(\tilde{\Psi}) = \nu(\tilde{\Psi}^{(J)}) \otimes \dots \otimes \nu(\tilde{\Psi}^{(0)}),$$

where

$$\bar{\Psi}^{(j)} := \begin{pmatrix} \bar{\psi}_1^1 & \dots & \bar{\psi}_{Q^{(j)}}^1 \\ \vdots & \ddots & \vdots \\ \bar{\psi}_1^{P^{(j)}} & \dots & \bar{\psi}_{Q^{(j)}}^{P^{(j)}} \end{pmatrix} \\ \nu(\tilde{\Psi}^{(j)}) := \begin{pmatrix} \tilde{\psi}_1^1 & \dots & \tilde{\psi}_1^{P^{(j)}} \\ \vdots & \ddots & \vdots \\ \tilde{\psi}_{Q^{(j)}}^1 & \dots & \tilde{\psi}_{Q^{(j)}}^{P^{(j)}} \end{pmatrix}.$$

and  $d^{(j)}, P^{(j)}$ , and  $Q^{(j)}$  are the filter lengths, the number of input channels, and the number of output channels for the  $j$ -th layer, respectively, which satisfies the condition (13) for the composite filter  $\tilde{\Psi}$  and  $\tilde{\Psi}$ .

Still, the deep convolutional framelet expansion is a linear representation, so we restricted the space  $\mathcal{H}^0$  in (18) so that the signal lives in the conic hull of the convolutional framelet basis to enable part-by-part representation similar to nonnegative matrix factorization (NMF) [46], [47], [47], [48] (see Appendix C in Supplementary Material for more detail), and we define it recursively:

$$\mathcal{H}^0 = \left\{ \mathbf{G} \in \mathbb{R}^{N \times 2} \mid \mathbf{G} = \left( \tilde{\Phi}^{(0)} \mathbf{C}^{(0)} \right) \otimes \nu(\tilde{\Psi}^{(0)}), \right. \\ \left. \mathbf{C}^{(0)} = \Phi^{(0)\top} \left( \mathbf{G} \otimes \bar{\Psi}^{(0)} \right) \in \mathcal{H}^1, \right. \\ \left. [\mathbf{C}^{(0)}]_{kl} \geq 0, \forall k, l \right\},$$

where  $\mathcal{H}^j$ ,  $j = 1, \dots, J-1$  is defined as

$$\mathcal{H}^j = \left\{ \mathbf{A} \in \mathbb{R}^{N \times P^{(j)}} \mid \mathbf{A} = \left( \tilde{\Phi}^{(j)} \mathbf{C}^{(j)} \right) \otimes \nu(\tilde{\Psi}^{(j)}), \right. \\ \left. \mathbf{C}^{(j)} = \Phi^{(j)\top} \left( \mathbf{A} \otimes \bar{\Psi}^{(j)} \right) \in \mathcal{H}^{j+1}, \right. \\ \left. [\mathbf{C}^{(j)}]_{kl} \geq 0, \forall k, l \right\} \\ \mathcal{H}^J = \mathbb{R}_+^{N \times P^{(L)}}. \quad (21)$$

This positivity constraint can be implemented using rectified linear unit (ReLU) during training. We call this version of generalization with ReLU and pooling layers as *DeepALOHA*.

## C. Sparsification

To further improve the performance of the structured matrix completion approach, in [34], we showed that even if the image  $x(\mathbf{r})$  may not be sparse, it can be often converted to an innovation signal using a shift-invariant transform represented by the whitening filter  $h$  such that the resulting innovation signal  $z = h * x$  becomes an FRI signal [36]. For example, many MR images can be sparsified using finite difference [28]. In this case, we can easily see that the Hankel matrix from the weighted  $k$ -space data,  $\hat{\mathbf{z}}(\mathbf{k}) = \hat{h}(\mathbf{k}) \hat{x}(\mathbf{k})$  are low-ranked, is low-ranked, where the weight  $\hat{h}(\mathbf{k})$  is determined from the

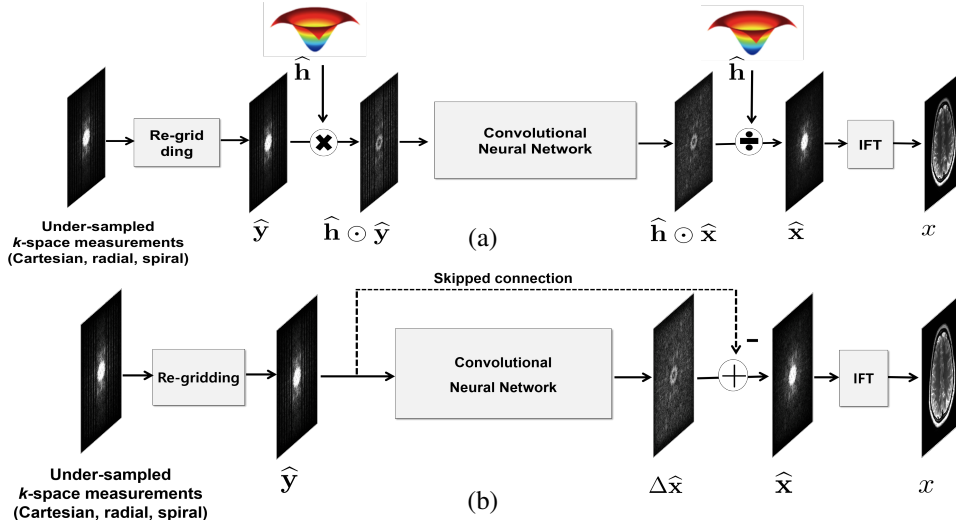


Fig. 2: Overall reconstruction flows of the proposed method with (a) weighting layers, and (b) skipped connection. IFT denotes the inverse Fourier transform.

finite difference or Haar wavelet transform [28], [34]. Thus, the deep neural network is applied to the weighted  $k$ -space data to estimate the missing spectral data  $\hat{h}(\mathbf{x})\hat{x}(\mathbf{k})$ , after which the original  $k$ -space data is obtained by dividing with the same weight, i.e.  $\hat{x}(\mathbf{k}) = \hat{z}(\mathbf{k})/\hat{h}(\mathbf{k})$ . As for the signal  $\hat{x}(\mathbf{k})$  at the spectral null of the filter  $\hat{h}(\mathbf{k})$ , the corresponding elements should be specifically obtained as sampled measurements, which can be easily done in MR acquisition (hence, without loss of generality, for the rest of the paper we assume that  $\hat{h}(\mathbf{k}_i) \neq 0$  for all  $i$ ). In DeepALOHA, this can be easily implemented using a weighting and unweighting layer as shown in Fig. 2(a).

Deep ALOHA allows another way to make the signal sparse. Note that fully sampled  $k$ -space data  $\hat{\mathbf{x}}$  can be represented by

$$\hat{\mathbf{x}} = \hat{\mathbf{y}} + \Delta\hat{\mathbf{x}},$$

where  $\hat{\mathbf{y}}$  is the undersampled  $k$ -space measurement in (3), and  $\Delta\hat{\mathbf{x}}$  is the residual part of  $k$ -space data that should be estimated. In practice, some of the low-frequency part of  $k$ -space data including the DC component are acquired in the undersampled measurement so that the image component from the residual  $k$ -space data  $\Delta\hat{\mathbf{x}}$  are mostly high frequency signals, which are sparse. Therefore,  $\Delta\hat{\mathbf{x}}$  has low-rank Hankel matrix structure, which can be effectively processed using the deep neural network. This can be easily implemented using a skipped connection before the deep neural network as shown in Fig. 2(b).

These two sparsification schemes can be combined for further performance improvement. Therefore, in this paper, we consider these three strategy to investigate which strategy is better for different sampling trajectories.

#### IV. IMPLEMENTATION

##### A. Overall Architecture

Since the Hankel matrix formulation in ALOHA implicitly assumes the Cartesian coordinate, to deal with the non-Cartesian sampling trajectories we add additional regriding

layers in front of the  $k$ -space weighting layer. Specifically, for radial and spiral trajectories, the non-uniform fast Fourier transform (NUFFT) was used to perform the regriding to the Cartesian coordinate. For Cartesian sampling trajectory, the regriding layer using NUFFT is not necessary, and we instead perform the nearest neighborhood interpolation to initially fill in the unacquired  $k$ -space regions.

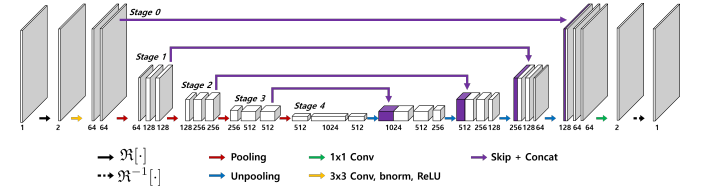


Fig. 3: A network backbone of the proposed method. The input and output are complex-valued.

##### B. Network Backbone

The network backbone follows the U-Net [3] which consists of convolution, batch normalization, rectified linear unit (ReLU), and contracting path connection with concatenation as shown in Fig. 3. Here, the input and output are the complex-valued  $k$ -space data, while  $\Re[\cdot]$  and  $\Im^{-1}[\cdot]$  denote the operators in (9) and (10), respectively, that convert complex valued input to two-channel real value signals and vice versa. The yellow arrow is the basic operator that consists of  $3 \times 3$  convolutions followed by a rectified linear unit (ReLU) and batch normalization. The same operation exists between the separate blocks at every stage, but the yellow arrows are omitted for visibility. A red and blue arrows are  $2 \times 2$  average pooling and average unpooling operators, respectively, located between the stages. A violet arrow is the skip and concatenation operator. A green arrow is the simple  $1 \times 1$  convolution operator generating interpolated  $k$ -space data from multichannel data.

### C. Network Training

We use the  $l_2$  loss in the image domain in ( $P'_A$ ) for training. For this, the Fourier transform operator is placed as the last layer to convert the interpolated  $k$ -space data to the complex-valued image domain so that the loss values are calculated for the reconstructed image. Stochastic gradient descent (SGD) optimizer was used to train the network. For the IFT layer, the adjoint operation from SGD is also Fourier transform. The size of mini batch was 4, and the number of epochs was 300. The initial learning rate was  $10^{-5}$ , which gradually dropped to  $10^{-6}$ . The regularization parameter was  $\lambda = 10^{-4}$ .

The labels for the network were the images generated from direct Fourier inversion from fully sampled  $k$ -space data. The input data for the network was the regridded down-sampled  $k$ -space data from Cartesian, radial, and spiral trajectories. The details of the downsampling procedure will be discussed later. For each trajectory, we train the network separately.

The proposed network was implemented using MatConvNet toolbox in MATLAB R2015a environment [49]. Processing units used in this research are Intel Core i7-7700 central processing unit and GTX 1080-Ti graphics processing unit. Training time lasted about 3 days.

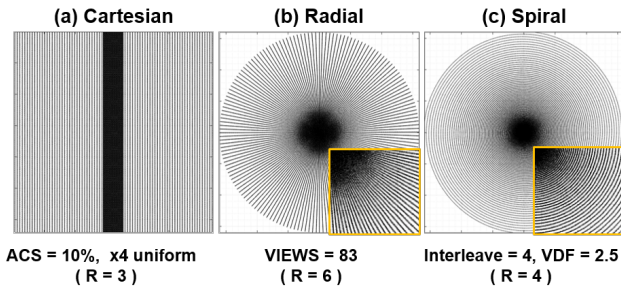


Fig. 4: Various under-sampling patterns: (a) Cartesian under-sampling at  $R = 3$ , (b) radial undersampling at  $R = 6$ , and (c) spiral undersampling at  $R = 4$ . Magnified views are provided for radial and spiral trajectories.

## V. MATERIAL AND METHODS

### A. Data Acquisition

For the Cartesian trajectory, knee  $k$ -space dataset (<http://mridata.org/>) were used. The raw data were acquired from 3D fast-spin-echo (FSE) sequence with proton density weighting included fat saturation comparison by a 3.0T whole body MR system (Discovery MR 750, DV22.0, GE Healthcare, Milwaukee, WI, USA). The repetition time (TR) and echo time (TE) were 1550 ms and 25 ms, respectively. There were 256 slices in total, and the thickness of each slice was 0.6 mm. The field of view (FOV) defined  $160 \times 160 \text{ mm}^2$  and the size of acquisition matrix is  $320 \times 320$ . The voxel size was 0.5 mm. The number of coils is 8. To evaluate the performance of the algorithm without using multi-coil data, coil compression (<http://mrsrl.stanford.edu/fao/software.html>) was applied to obtain a single coil  $k$ -space data. For the Cartesian trajectory as shown in Fig. 4(a), the input  $k$ -space was uniformly down-sampled using x4 acceleration factor

in addition to the 10% autocalibration signal (ACS) line. Therefore, the net acceleration factor is about 3 ( $R = 3$ ). Among the 20 cases of knee data, 18 cases were used for training, 1 case for validation, and the other for test.

For radial and spiral sampling patterns, a synthesized  $k$ -space data from Human Connectome Project (HCP) MR dataset (<https://db.humanconnectome.org>) were used. Specifically, the radial and spiral  $k$ -space data are generated using MRI simulator (<http://bigwww.epfl.ch/algorithms/mri-reconstruction/>). The T2 weighted brain images contained within the HCP were acquired Siemens 3T MR system using a 3D spin-echo sequence. The TR and TE were 3200 ms and 565 ms, respectively. The number of coils was 32, but the final reconstruction was obtained as the sum of the squares. Our synthesized  $k$ -space data for single coil data were generated from the final reconstruction image. The FOV was  $224 \times 224 \text{ mm}^2$ , and the size of acquisition matrix was  $320 \times 320$ . The voxel size was 0.7 mm. The total of 199 subject datasets was used in this paper. Among the 199 subject, 180 were used for network training, 10 subject for validation, and the other subject for test. Fig. 4(b) shows the down-sampled  $k$ -space radial sampling patterns. The downsampled radial  $k$ -space consists of only 83 spokes, which corresponds to  $R = 6$  acceleration factor compared to the 503 spokes for the fully sampled data that were used as the ground-truth. On the other hand, Fig. 4(c) shows the down-sampled spiral sampling pattern, composed of 4 interleaves that corresponds to  $R = 4$  acceleration compared to the full spiral trajectory with 16 interleaves. The spiral  $k$ -space trajectory was obtained with a variable density factor (VDF) of 2.5.

### B. Performance Evaluation

For quantitative evaluation, the normalized mean square error (NMSE) value was used, which is defined as

$$NMSE = \frac{\sum_{i=1}^M \sum_{j=1}^N [x^*(i, j) - x(i, j)]^2}{\sum_{i=1}^M \sum_{j=1}^N [x^*(i, j)]^2}, \quad (22)$$

where  $x$  and  $x^*$  denote the reconstructed images and ground truth, respectively.  $M$  and  $N$  are the number of pixel for row and column. We also use the peak signal to noise ratio (PSNR), which is defined by

$$PSNR = 20 \cdot \log_{10} \left( \frac{NM \|x^*\|_{\infty}}{\|x - x^*\|_2} \right). \quad (23)$$

We also use the structural similarity (SSIM) index [50], defined as

$$SSIM = \frac{(2\mu_x \mu_{x^*} + c_1)(2\sigma_{xx^*} + c_2)}{(\mu_x^2 + \mu_{x^*}^2 + c_1)(\sigma_x^2 + \sigma_{x^*}^2 + c_2)}, \quad (24)$$

where  $\mu_x$  is a average of  $x$ ,  $\sigma_x^2$  is a variance of  $x$  and  $\sigma_{xx^*}$  is a covariance of  $x$  and  $x^*$ . There are two variables to stabilize the division such as  $c_1 = (k_1 L)^2$  and  $c_2 = (k_2 L)^2$ .  $L$  is a dynamic range of the pixel intensities.  $k_1$  and  $k_2$  are constants by default  $k_1 = 0.01$  and  $k_2 = 0.03$ .

As a reference architecture for comparison, the image domain residual learning using the standard U-Net backbone in Fig. 3 was used. Unlike the proposed network, the input and

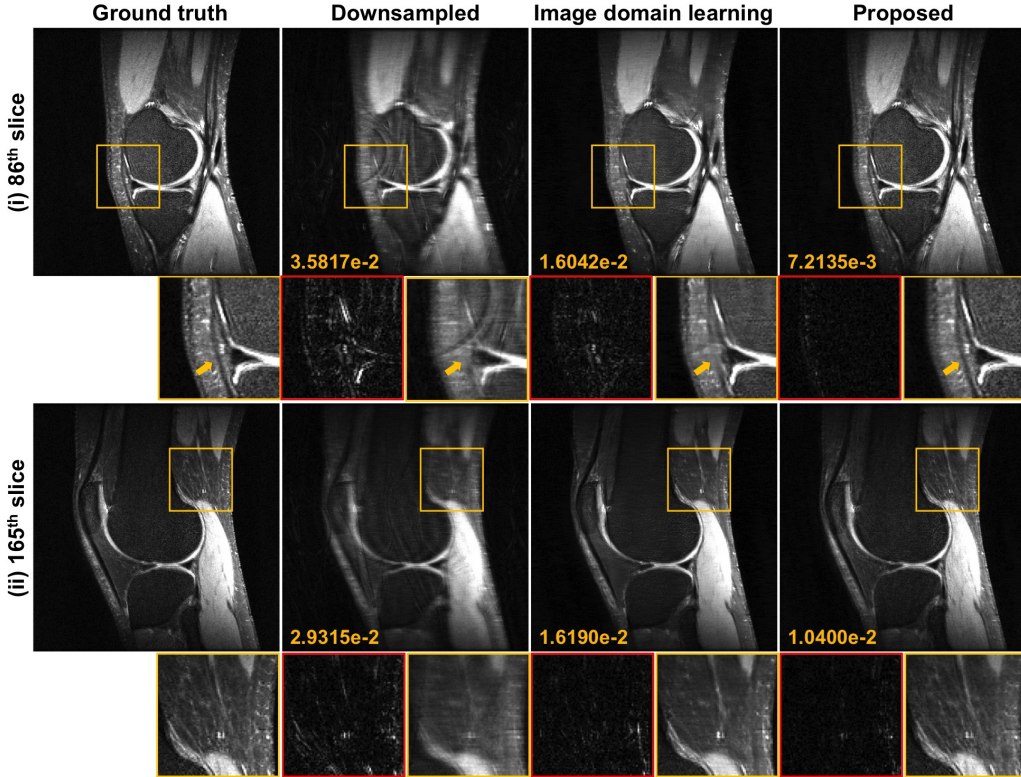


Fig. 5: Reconstruction results from Cartesian trajectory at  $R = 3$ . The difference images were amplified five times. Yellow and red boxes illustrate the enlarged and difference views, respectively. The number written to the images is the NMSE value.

output are an artifact image and artifact-only image, respectively. This architecture has been popularly used to remove the aliasing artifacts from the artifact corrected imagers [12]. The image domain residual network was trained using the same hyper-parameter as the training of the proposed network except for the number of epochs and the learning rate. In the image domain reference network, the number of epochs is 500 and the learning rate gradually decreases from  $10^{-4}$  to  $10^{-5}$ , until the 300-th epochs.

## VI. RESULTS

Fig. 5 shows the reconstruction results from Cartesian trajectory using the architecture in Fig. 2(a) combined with the skipped connection as Fig. 2(b). As shown in the enlarged images and difference images, the image-domain residual network resulted in the blurry edges and textures in several area, while DeepALOHA accurately recovered high frequency edges and textures. Fig. 6 shows the reformed images along the axial direction, after all the reconstruction was done along the sagittal direction. The reformatted axial image preserved the detailed structures of underlying images without any artifact along the slice direction. The quantitative comparison in Table I in terms of average PSNR, NMSE, and SSIM value also confirmed that the proposed  $k$ -space interpolation method produced the best quantitative values in all area.

Metric	Input	Image domain learning	DeepALOHA
PSNR [dB]	31.0201	33.3799	35.5181
NMSE ( $\times 10^{-2}$ )	5.9156	4.6989	3.0039
SSIM	0.6705	0.7719	0.8459

TABLE I: Quantitative comparison from Cartesian trajectory at  $R = 3$ .

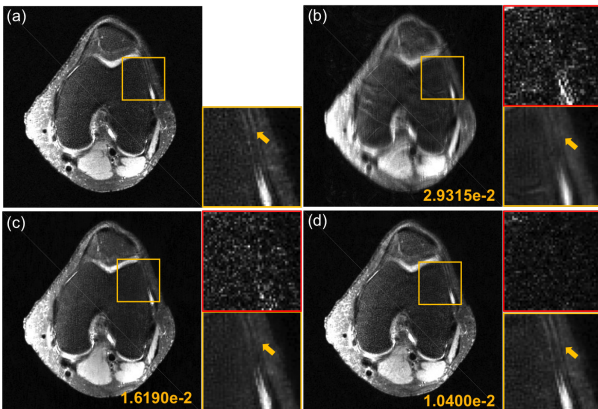


Fig. 6: Axial reformed reconstruction results from Cartesian trajectory at  $R = 3$ : (a) ground-truth, (b) downsampled, (c) image-domain learning and (d) the proposed method. The number written to the images is the NMSE value.

Fig. 7 shows the reconstruction images from x6 accelerated radial sampling patterns using the architecture in Fig. 2(b). DeepALOHA provided realistic image quality and preserves the detailed structures as well as the textures, but the image domain network failed to preserve the realistic textures and sophisticated structures. It also provides much smallest NMSE

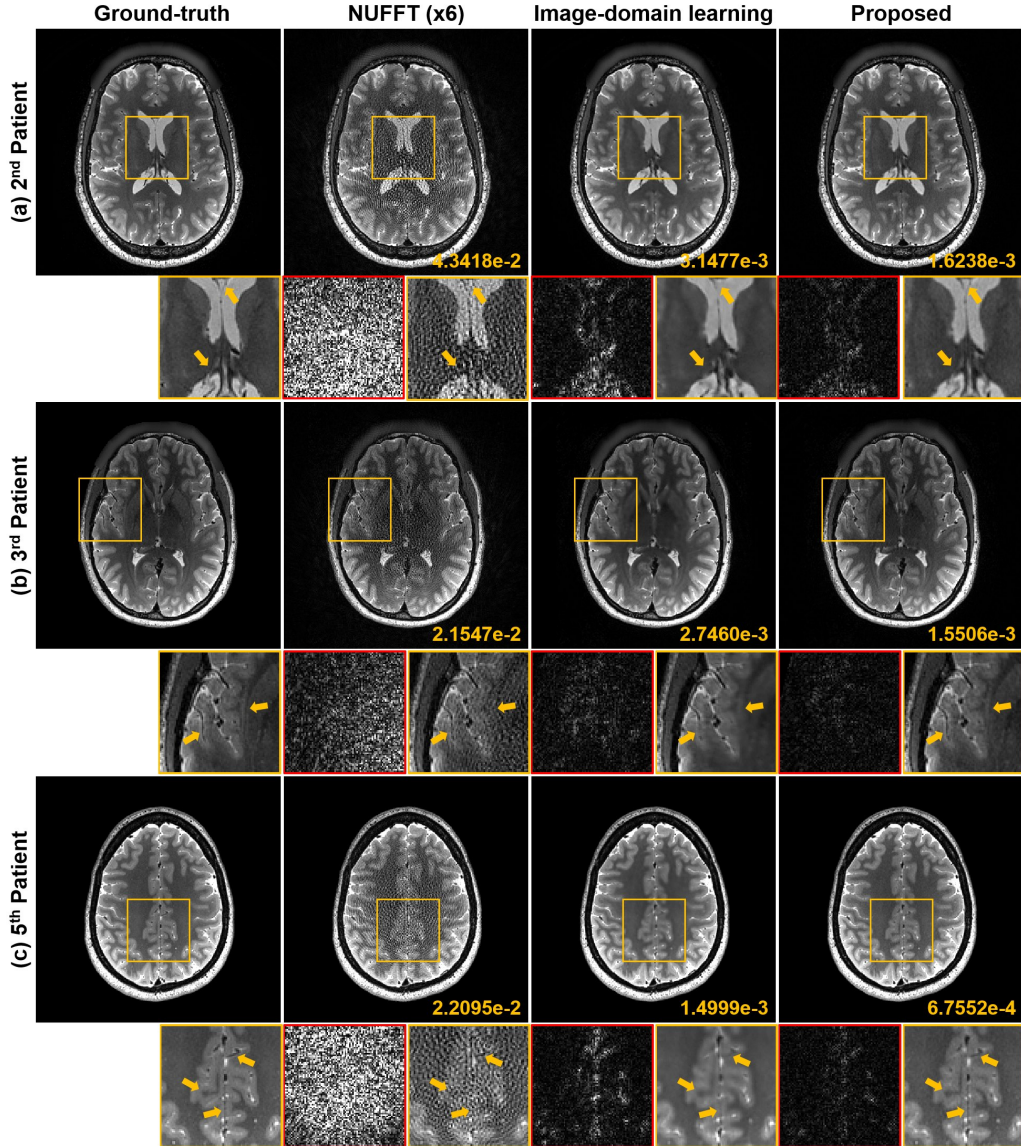


Fig. 7: Reconstruction results from radial trajectory at  $R = 6$ . The difference images were amplified five times. Yellow and red boxes illustrate the enlarged and difference views, respectively. The number written to the images is the NMSE value.

values, as shown at the bottom of each Fig. 7. Average PSNR and SSIM values are shown in Table II. The average values were calculated across all slices and 9 subjects. DeepALOHA provided the best PSNR and SSIM values. Although DeepALOHA provided slight worse SSIM values in the whole image area, its SSIM values within the brain region outperformed the image-domain network as shown in Table II(b). This was because the SSIM calculation for the whole area are mostly biased to the flat background region, which is well reconstructed by the image domain network. However, the diagnostically important features are within the brain region, in which  $k$ -space learning using DeepALOHA was superior.

Fig. 8 shows the reconstruction images from x4 accelerated spiral trajectory using the architecture in Fig. 2(a). Similar to the radial sampling patterns, the proposed method provides significantly improved image reconstruction results, and the

	Metric	Input	Image-domain learning	DeepALOHA
(a)	PSNR [dB]	30.6443	41.4220	43.6502
	SSIM	0.6659	0.9779	0.9729
(b)	PSNR [dB]	31.2755	41.6157	44.1446
	SSIM	0.8736	0.9815	0.9876

TABLE II: Quantitative comparison from radial undersampling at  $R = 6$ : (a) whole image area and (b) within body.

average PSNR and SSIM values in Table III also confirm that the proposed method consistently outperform the image-domain network for all patients in all area.

	Metric	Input	Image domain learning	DeepALOHA
	PSNR [dB]	30.6760	41.9122	44.5396
	SSIM	0.88163	0.9807	0.9898

TABLE III: Quantitative comparison from spiral undersampling at  $R = 4$ .

## VII. CONCLUSION

Inspired by the close theoretical link between the ALOHA and deep learning, this paper showed that fully data-driven  $k$ -space interpolation is feasible by using  $k$ -space deep learning and the image domain loss function. The proposed  $k$ -space interpolation network significantly outperformed the existing image domain deep learning for various sampling trajectory.

In addition, our theory and numerical verification can address some of the fundamental questions that we raised at Introduction. Specifically, the current practice of splitting real and imaginary channels is valid for  $k$ -space interpolation since it preserves the low-rank nature of the Hankel structured matrix. Moreover, our theoretical analysis confirmed that we do not need to re-invent a new nonlinearity for complex-valued MR image reconstruction problems, since the main role of the positivity constraint from ReLU is to enable conic decomposition using framelet basis. Finally, we showed that the number of filter channels controls the low-rank structure of the feasible solutions for the given regression problems. As the proposed  $k$ -space interpolation framework is quite effective and also supported by novel theory, so we believe that this opens a new area of researches for many Fourier imaging problems.

## REFERENCES

- [1] A. Krizhevsky, I. Sutskever, and G. E. Hinton, "Imagenet classification with deep convolutional neural networks," in *Advances in neural information processing systems*, 2012, pp. 1097–1105.
- [2] K. He, X. Zhang, S. Ren, and J. Sun, "Deep residual learning for image recognition," in *Proceedings of the IEEE Conference on Computer Vision and Pattern Recognition*, 2016, pp. 770–778.
- [3] O. Ronneberger, P. Fischer, and T. Brox, "U-net: Convolutional networks for biomedical image segmentation," in *International Conference on Medical Image Computing and Computer-Assisted Intervention*. Springer, 2015, pp. 234–241.
- [4] K. Zhang, W. Zuo, Y. Chen, D. Meng, and L. Zhang, "Beyond a gaussian denoiser: Residual learning of deep CNN for image denoising," *arXiv preprint arXiv:1608.03981*, 2016.
- [5] J. Kim, J. Kwon Lee, and K. Mu Lee, "Accurate image super-resolution using very deep convolutional networks," in *Proceedings of the IEEE Conference on Computer Vision and Pattern Recognition*, 2016, pp. 1646–1654.
- [6] E. Kang, J. Min, and J. C. Ye, "A deep convolutional neural network using directional wavelets for low-dose X-ray CT reconstruction," *Medical physics*, vol. 44, no. 10, 2017.
- [7] H. Chen, Y. Zhang, M. K. Kalra, F. Lin, Y. Chen, P. Liao, J. Zhou, and G. Wang, "Low-dose ct with a residual encoder-decoder convolutional neural network," *IEEE transactions on medical imaging*, vol. 36, no. 12, pp. 2524–2535, 2017.
- [8] E. Kang, W. Chang, J. Yoo, and J. C. Ye, "Deep convolutional framelet denoising for low-dose CT via wavelet residual network," *IEEE Transactions on Medical Imaging (in press)*, 2018.
- [9] H. Chen, Y. Zhang, W. Zhang, P. Liao, K. Li, J. Zhou, and G. Wang, "Low-dose CT via convolutional neural network," *Biomedical Optics Express*, vol. 8, no. 2, pp. 679–694, 2017.
- [10] J. Adler and O. Öktem, "Learned primal-dual reconstruction," *IEEE Transactions on Medical Imaging (in press)*, 2018.
- [11] J. M. Wolterink, T. Leiner, M. A. Viergever, and I. Išgum, "Generative adversarial networks for noise reduction in low-dose CT," *IEEE Transactions on Medical Imaging*, vol. 36, no. 12, pp. 2536–2545, 2017.
- [12] K. H. Jin, M. T. McCann, E. Froustey, and M. Unser, "Deep convolutional neural network for inverse problems in imaging," *IEEE Transactions on Image Processing*, vol. 26, no. 9, pp. 4509–4522, 2017.
- [13] Y. Han and J. C. Ye, "Framing U-Net via Deep Convolutional Framelets: Application to Sparse-view CT," *IEEE Transactions on Medical Imaging (in press)*, 2018.
- [14] S. Wang, Z. Su, L. Ying, X. Peng, S. Zhu, F. Liang, D. Feng, and D. Liang, "Accelerating magnetic resonance imaging via deep learning," in *Biomedical Imaging (ISBI), 2016 IEEE 13th International Symposium on*. IEEE, 2016, pp. 514–517.
- [15] K. Hammernik, T. Klatzer, E. Kobler, M. P. Recht, D. K. Sodickson, T. Pock, and F. Knoll, "Learning a variational network for reconstruction of accelerated MRI data," *Magnetic resonance in medicine*, vol. 79, no. 6, pp. 3055–3071, 2018.
- [16] K. Kwon, D. Kim, and H. Park, "A parallel MR imaging method using multilayer perceptron," *Medical physics*, vol. 44, no. 12, pp. 6209–6224, 2017.
- [17] D. Lee, J. Yoo, S. Tak, and J. Ye, "Deep residual learning for accelerated MRI using magnitude and phase networks," *IEEE Transactions on Biomedical Engineering*, 2018.
- [18] Y. S. Han, J. Yoo, and J. C. Ye, "Deep learning with domain adaptation for accelerated projection reconstruction MR," *Magnetic Resonance in Medicine*, <https://doi.org/10.1002/mrm.27106>, 2018.
- [19] J. Schlemper, J. Caballero, J. V. Hajnal, A. N. Price, and D. Rueckert, "A deep cascade of convolutional neural networks for dynamic mr image reconstruction," *IEEE transactions on Medical Imaging*, vol. 37, no. 2, pp. 491–503, 2018.
- [20] T. M. Quan, T. Nguyen-Duc, and W.-K. Jeong, "Compressed sensing MRI reconstruction using a generative adversarial network with a cyclic loss," *IEEE Transactions on Medical Imaging (in press)*, 2018.
- [21] B. Zhu, J. Z. Liu, S. F. Cauley, B. R. Rosen, and M. S. Rosen, "Image reconstruction by domain-transform manifold learning," *Nature*, vol. 555, no. 7697, p. 487, 2018.
- [22] M. Lustig, D. Donoho, and J. Pauly, "Sparse MRI: The application of compressed sensing for rapid mr imaging," *Magnetic Resonance in Medicine*, vol. 58, no. 6, pp. 1182–1195, 2007.
- [23] M. Lustig and J. M. Pauly, "SPIRiT: Iterative self-consistent parallel imaging reconstruction from arbitrary k-space," *Magnetic resonance in medicine*, vol. 64, no. 2, pp. 457–471, 2010.
- [24] H. Jung, K. Sung, K. Nayak, E. Kim, and J. Ye, "k-t FOCUSS: A general compressed sensing framework for high resolution dynamic MRI," *Magnetic Resonance in Medicine*, vol. 61, no. 1, pp. 103–116, 2009.
- [25] S. Lingala, Y. Hu, E. DiBella, and M. Jacob, "Accelerated dynamic MRI exploiting sparsity and low-rank structure: kt slr," *IEEE Trans. on Medical Imaging*, vol. 30, no. 5, pp. 1042–1054, 2011.
- [26] P. J. Shin, P. E. Larson, M. A. Ohliger, M. Elad, J. M. Pauly, D. B. Vigneron, and M. Lustig, "Calibrationless parallel imaging reconstruction based on structured low-rank matrix completion," *Magnetic resonance in medicine*, vol. 72, no. 4, pp. 959–970, 2014.
- [27] J. P. Haldar, "Low-rank modeling of local  $k$ -space neighborhoods (loraks) for constrained mri," *IEEE transactions on medical imaging*, vol. 33, no. 3, pp. 668–681, 2014.
- [28] K. H. Jin, D. Lee, and J. C. Ye, "A general framework for compressed sensing and parallel MRI using annihilating filter based low-rank Hankel matrix," *IEEE Transactions on Computational Imaging*, vol. 2, no. 4, pp. 480–495, 2016.
- [29] D. Lee, K. H. Jin, E. Y. Kim, S.-H. Park, and J. C. Ye, "Acceleration of mr parameter mapping using annihilating filter-based low rank hankel matrix (aloha)," *Magnetic resonance in medicine*, vol. 76, no. 6, pp. 1848–1864, 2016.
- [30] J. Lee, K. H. Jin, and J. C. Ye, "Reference-free single-pass EPI Nyquist ghost correction using annihilating filter-based low rank Hankel matrix (ALOHA)," *Magnetic resonance in medicine*, vol. 76, no. 6, pp. 1775–1789, 2016.
- [31] G. Ongie and M. Jacob, "Off-the-grid recovery of piecewise constant images from few Fourier samples," *SIAM Journal on Imaging Sciences*, vol. 9, no. 3, pp. 1004–1041, 2016.
- [32] D. L. Donoho, "Compressed sensing," *IEEE Trans. on Information Theory*, vol. 52, no. 4, pp. 1289–1306, April 2006.
- [33] E. Candes, J. Romberg, and T. Tao, "Robust uncertainty principles: Exact signal reconstruction from highly incomplete frequency information," *IEEE Trans. on Information Theory*, vol. 52, no. 2, pp. 489–509, Feb. 2006.
- [34] J. C. Ye, J. M. Kim, K. H. Jin, and K. Lee, "Compressive sampling using annihilating filter-based low-rank interpolation," *IEEE Transactions on Information Theory*, vol. 63, no. 2, pp. 777–801, Feb. 2017.
- [35] J. C. Ye, Y. S. Han, and E. Cha, "Deep convolutional framelets: A general deep learning framework for inverse problems," *SIAM Journal on Imaging Sciences (in press)*, also available as *arXiv preprint arXiv:1707.00372*, 2018.

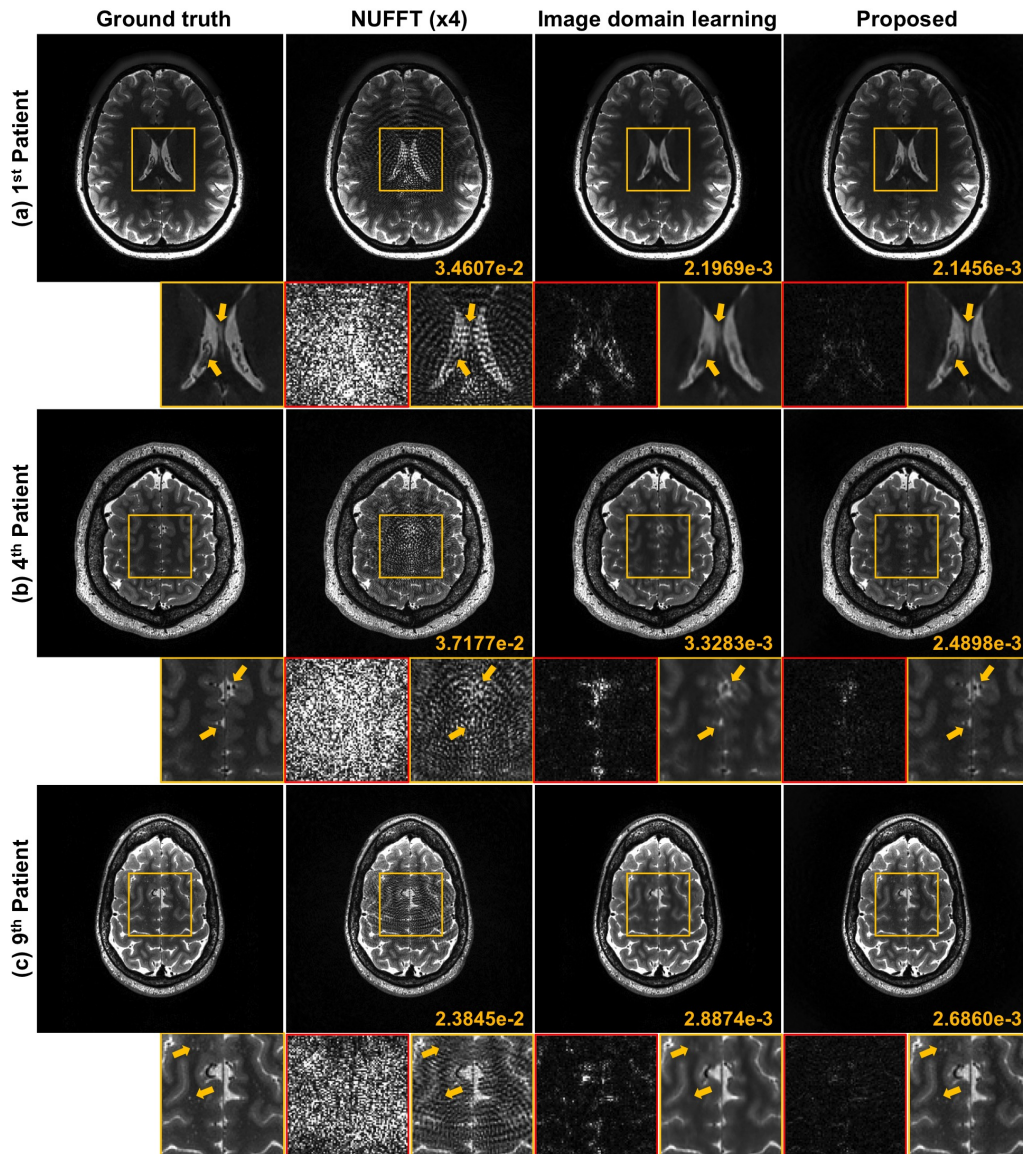


Fig. 8: Reconstruction results from spiral trajectory at  $R = 4$ . The difference images were amplified five times. Yellow and red boxes illustrate the enlarged and difference views, respectively. The number written to the images is the NMSE value.

- [36] M. Vetterli, P. Marziliano, and T. Blu, "Sampling signals with finite rate of innovation," *IEEE Transactions on Signal Processing*, vol. 50, no. 6, pp. 1417–1428, 2002.
- [37] E. J. Candès and B. Recht, "Exact matrix completion via convex optimization," *Foundations of Computational mathematics*, vol. 9, no. 6, p. 717, 2009.
- [38] J.-F. Cai, E. J. Candès, and Z. Shen, "A singular value thresholding algorithm for matrix completion," *SIAM Journal on Optimization*, vol. 20, no. 4, pp. 1956–1982, 2010.
- [39] E. J. Candès and T. Tao, "The power of convex relaxation: Near-optimal matrix completion," *IEEE Trans. on Information Theory*, vol. 56, no. 5, pp. 2053–2080, 2010.
- [40] D. Gross, "Recovering low-rank matrices from few coefficients in any basis," *IEEE Transactions on Information Theory*, vol. 57, no. 3, pp. 1548–1566, 2011.
- [41] R. H. Keshavan, A. Montanari, and S. Oh, "Matrix completion from a few entries," *IEEE Trans. on Information Theory*, vol. 56, no. 6, pp. 2980–2998, 2010.
- [42] K. H. Jin, J.-Y. Um, D. Lee, J. Lee, S.-H. Park, and J. C. Ye, "Mri artifact correction using sparse+ low-rank decomposition of annihilating filter-based Hankel matrix," *Magnetic resonance in medicine*, vol. 78, no. 1, pp. 327–340, 2017.
- [43] K. H. Jin and J. C. Ye, "Annihilating filter-based low-rank Hankel matrix approach for image inpainting," *IEEE Transactions on Image Processing*, vol. 24, no. 11, pp. 3498–3511, 2015.
- [44] —, "Sparse and low-rank decomposition of a Hankel structured matrix for impulse noise removal," *IEEE Transactions on Image Processing*, vol. 27, no. 3, pp. 11448–1461, 2018.
- [45] G. Ongie and M. Jacob, "A fast algorithm for convolutional structured low-rank matrix recovery," *IEEE Transactions on Computational Imaging*, vol. 3, no. 4, pp. 535–550, 2017.
- [46] D. D. Lee and H. S. Seung, "Unsupervised learning by convex and conic coding," in *Advances in neural information processing systems*, 1997, pp. 515–521.
- [47] —, "Learning the parts of objects by non-negative matrix factorization," *Nature*, vol. 401, no. 6755, p. 788, 1999.
- [48] —, "Algorithms for non-negative matrix factorization," in *Advances in neural information processing systems*, 2001, pp. 556–562.
- [49] A. Vedaldi and K. Lenc, "Matconvnet: Convolutional neural networks for Matlab," in *Proceedings of the 23rd ACM international conference on Multimedia*. ACM, 2015, pp. 689–692.
- [50] Z. Wang, A. C. Bovik, H. R. Sheikh, and E. P. Simoncelli, "Image quality assessment: from error visibility to structural similarity," *IEEE transactions on image processing*, vol. 13, no. 4, pp. 600–612, 2004.

## SUPPLEMENTARY MATERIAL

### APPENDIX A

For simplicity, here we consider 1-D signals, but its extension to 2-D is straightforward. In addition, to avoid separate treatment of boundary conditions, we assume periodic boundary. Let  $\mathbf{f} \in \mathbb{C}^N$  be the signal vector. Then, a single-input single-output (SISO) convolution of the input  $\mathbf{f}$  and the filter  $\bar{\mathbf{h}}$  can be represented in a matrix form:

$$\mathbf{y} = \mathbf{f} \circledast \bar{\mathbf{h}} = \mathbb{H}_d(\mathbf{f})\mathbf{h}, \quad (25)$$

where  $\mathbb{H}_d(\mathbf{f})$  is a wrap-around Hankel matrix defined by

$$\mathbb{H}_d(\mathbf{f}) = \begin{bmatrix} [\mathbf{f}]_1 & [\mathbf{f}]_2 & \cdots & [\mathbf{f}]_d \\ [\mathbf{f}]_2 & [\mathbf{f}]_3 & \cdots & [\mathbf{f}]_{d+1} \\ \vdots & \vdots & \ddots & \vdots \\ [\mathbf{f}]_N & [\mathbf{f}]_1 & \cdots & [\mathbf{f}]_{d-1} \end{bmatrix} \quad (26)$$

where  $d$  denotes the matrix pencil parameter. On the other hand, multi-input multi-output (MIMO) convolution for the  $P$ -channel input  $\mathbf{Z} = [\mathbf{z}_1, \dots, \mathbf{z}_P]$  to generate  $Q$ -channel output  $\mathbf{Y} = [\mathbf{y}_1, \dots, \mathbf{y}_Q]$  can be represented by

$$\mathbf{y}_i = \sum_{j=1}^P \mathbf{z}_j \circledast \bar{\psi}_i^j, \quad i = 1, \dots, Q \quad (27)$$

where  $\bar{\psi}_i^j \in \mathbb{R}^d$  denotes the length  $d$ -filter that convolves the  $j$ -th channel input to compute its contribution to the  $i$ -th output channel. By defining the MIMO filter kernel  $\Psi$  as follows:

$$\Psi = \begin{bmatrix} \Psi_1 \\ \vdots \\ \Psi_P \end{bmatrix} \quad \text{where} \quad \Psi_j = [\psi_1^j \quad \cdots \quad \psi_Q^j] \in \mathbb{R}^{d \times Q} \quad (28)$$

the corresponding matrix representation of the MIMO convolution is then given by

$$\mathbf{Y} = \mathbf{Z} \circledast \bar{\Psi} \quad (29)$$

$$= \sum_{j=1}^P \mathbb{H}_d(\mathbf{z}_j) \Psi_j \quad (30)$$

$$= \mathbb{H}_{d|P}(\mathbf{Z}) \Psi \quad (31)$$

where  $\bar{\Psi}$  is a flipped block structured matrix:

$$\bar{\Psi} = \begin{bmatrix} \bar{\Psi}_1 \\ \vdots \\ \bar{\Psi}_P \end{bmatrix} \quad \text{where} \quad \bar{\Psi}_j = [\bar{\psi}_1^j \quad \cdots \quad \bar{\psi}_Q^j] \in \mathbb{R}^{d \times Q} \quad (32)$$

and  $\mathbb{H}_{d|P}(\mathbf{Z})$  is an *extended Hankel matrix* by stacking  $P$  Hankel matrices side by side:

$$\mathbb{H}_{d|P}(\mathbf{Z}) := [\mathbb{H}_d(\mathbf{z}_1) \quad \mathbb{H}_d(\mathbf{z}_2) \quad \cdots \quad \mathbb{H}_d(\mathbf{z}_P)] \quad (33)$$

### APPENDIX B

For a given  $\mathbf{f} \in \mathbb{C}^N$ , let

$$\mathbf{B} := \begin{bmatrix} \text{Re} [\mathbb{H}_d(\mathbf{f})] & \text{Im} [\mathbb{H}_d(\mathbf{f})] \\ -\text{Im} [\mathbb{H}_d(\mathbf{f})] & \text{Re} [\mathbb{H}_d(\mathbf{f})] \end{bmatrix}$$

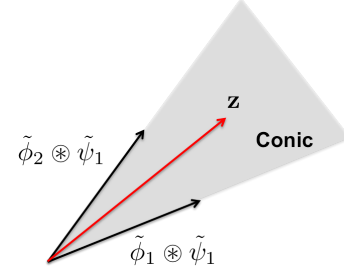


Fig. 9: Example of conic coding in DeepALOHA. A 2-dimensional vector  $\mathbf{z}$  lies the conic hull of two convolution framelet basis when  $N = 2, Q = 1$ .

and

$$\mathbf{T} = \frac{1}{\sqrt{2}} \begin{bmatrix} \mathbf{I}_N & \mathbf{I}_N \\ \iota \mathbf{I}_N & -\iota \mathbf{I}_N \end{bmatrix}.$$

Then, we can easily see that  $\mathbf{T}$  is an orthonormal matrix and

$$\mathbf{T}^\top \mathbf{B} \mathbf{T} = \begin{bmatrix} \mathbb{H}_d(\mathbf{f}) & 0 \\ 0 & \mathbb{H}_d^*(\mathbf{f}) \end{bmatrix},$$

which leads to

$$\begin{aligned} \text{RANK} \begin{bmatrix} \text{Re} [\mathbb{H}_d(\mathbf{f})] & \text{Im} [\mathbb{H}_d(\mathbf{f})] \\ -\text{Im} [\mathbb{H}_d(\mathbf{f})] & \text{Re} [\mathbb{H}_d(\mathbf{f})] \end{bmatrix} \\ = \text{RANK} \mathbb{H}_d(\mathbf{f}) + \text{RANK} \mathbb{H}_d^*(\mathbf{f}) = 2 \text{RANK} \mathbb{H}_d(\mathbf{f}). \end{aligned}$$

Therefore,

$$\text{RANK} [\text{Re} [\mathbb{H}_d(\mathbf{f})] \quad \text{Im} [\mathbb{H}_d(\mathbf{f})]] \leq 2 \text{RANK} \mathbb{H}_d(\mathbf{f}).$$

### APPENDIX C

Then, using (13) and (14), the convolution framelet coefficient  $\mathbf{C} \in \mathbb{R}^{M \times Q}$  is defined by

$$\mathbf{C} = \Phi^\top \mathbb{H}_{d|P}(\mathbf{Z}) \Psi = \Phi^\top (\mathbf{Z} \circledast \bar{\Psi})$$

and its  $(i, j)$ -th element is given by [35]:

$$c_{ij} = \phi_i^\top \mathbb{H}_{d|P}(\mathbf{Z}) \psi_j = \sum_{k=1}^P \langle \mathbf{z}_k, \phi_i \circledast \psi_j^k \rangle$$

Then, we have the following convolution framelet decomposition [35]:

$$\mathbf{z}_m = \frac{1}{d} \sum_{i=1}^N \sum_{j=1}^Q c_{ij} (\tilde{\phi}_i \circledast \tilde{\psi}_j^m), \quad m = 1, \dots, P. \quad (34)$$

This means that  $\{\tilde{\phi}_i \circledast \tilde{\psi}_j^m\}$  becomes the frame basis, and the expansion coefficients becomes  $\{c_{ij}\}$ .

Furthermore, under the ReLU (i.e.  $c_{ij} \geq 0$ ), (34) implies that  $\mathbf{z}_m$  can be represented as a positive combination of the frame basis as illustrated in Fig. 9. This so-called *conic coding* is well-known to learn part by part representation of objects [46], [47], which constitutes the key ingredient of nonnegative matrix factorization (NMF) [47], [48].